Supporting Information for: On-Demand Generation of Indistinguishable Photons in the Telecom C-Band Using Quantum Dot Devices

Daniel A. Vajner,[†] Paweł Holewa,[‡,¶,§] Emilia Zięba-Ostój,[‡] Maja Wasiluk,[‡]

Martin von Helversen,[†] Aurimas Sakanas,[¶] Alexander Huck,[‖] Kresten Yvind,[¶,§]

Niels Gregersen,[¶] Anna Musiał,[‡] Marcin Syperek,[‡] Elizaveta Semenova,[¶,§] and

Tobias Heindel[*,†]

[†]Institute of Solid State Physics, Technical University of Berlin, 10623 Berlin, Germany

[‡]Department of Experimental Physics, Faculty of Fundamental Problems of Technology, Wrocław University of Science and Technology, 50-370 Wrocław, Poland

[¶]DTU Electro, Department of Electrical and Photonics Engineering, Technical University of Denmark, Kongens Lyngby 2800, Denmark

[§]NanoPhoton - Center for Nanophotonics, Technical University of Denmark, 2800 Kongens Lyngby, Denmark

[‖]Center for Macroscopic Quantum States (bigQ), Department of Physics, Technical University of Denmark, 2800 Kgs. Lyngby, Denmark

E-mail: tobias.heindel@tu-berlin.de

Contents

1 Quantum Dot Characterization

1.1 Sample Fabrication

The QD structure was grown on (001)-oriented InP substrate by metal-organic vapour phase epitaxy (MOVPE). The array of low surface density ($\sim 2.8 \times 10^9 \text{cm}^{-2}$) InAs QDs was placed in the centre of a 488 nm thick InP layer grown on a 200 nm-thick InGaAs sacrificial layer lattice-matched to InP. Subsequently, 100 nm thick SiO_2 followed by a 100-nm-thick metallic reflector were deposited onto InP surface, and then bonded to a Si substrate using benzocyclobutene (BCB). Finally, the InP substrate and sacrificial layer were removed. To fabricate mesas, we used electron beam lithography followed by inductively coupled plasma-reactive ion etching. For more details we refer to Ref. 1.

1.2 Identification of Excitonic Complexes

This section provides additional experimental data supporting the assignment of the excitonic states of the QD investigated in the main article. The measurements shown in Supplemental Information (SI) Figure S1 were performed under above-barrier continuous wave (CW) excitation using a 980 nm laser diode. The assignment of emission lines to the biexciton (XX) and exciton (X) state of the QD is confirmed by polarization- (cf. Figure S1(a)) and excitation-power dependent (cf. Figure S1(b)) photoluminescence measurements collecting only emission from the single QD device (µPL). The identification of the excitonic complexes is further supported by XX-X photon cross-correlation measurements (cf. Figure S1(c)). The polarization-resolved µPL spectra reveal a fine-structure splitting (FSS) of the X state of $(88 \pm 2)\,\mu\text{eV}$ in line with Ref. 1. Moreover, analyzing the total X and XX emission intensity as a function of the detection polarization, a degree of linear polarization (DOP) of 33% can be inferred from the oscillation contrast (cf. Figure S1(a), Inset). The excitation-power dependent µPL, presented in double-logarithmic scaling, reveals a saturation of the X emission (blue line), a super-linear increase of the XX emission (green line) at high power and a monotonic behavior of the trion emission (black line). Not least, the cascaded emission of

3

XX- and X-photons is confirmed by the asymmetric photon cross-correlation signature in Figure S1(c).
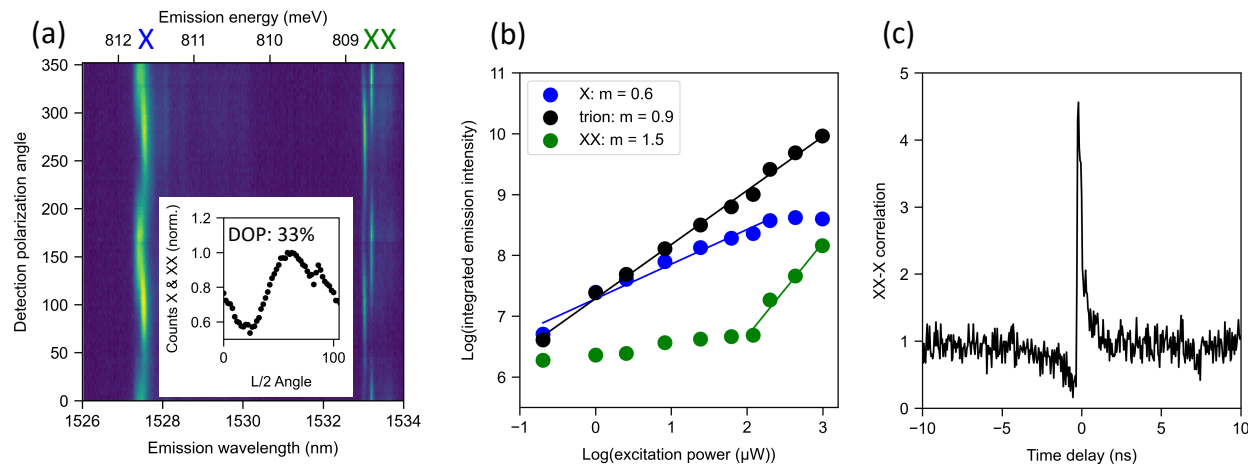

Figure S1: Identification of excitonic complexes under above-barrier excitation: (a) Micro-photoluminescence spectra as a function of the angle between a $\lambda/2$-waveplate and an analyzing polarizer, revealing a fine-structure splitting (FSS) of the biexciton (XX) and exciton (X) emission doublets. Inset: Summed integrated intensity of XX and X emission for extraction of the degree of linear polarization (DOP). (b) Integrated emission intensities of XX, X, and trion-state as a function of the excitation power. (c) Photon cross-correlation histogram using the XX-photons as 'start' and X-photons as 'stop'.

1.3   Linewidth under Two-Photon-Excitation

To extract the QD emission linewidths under TPE, we perform Gaussian fits of the X and XX emission line (see Figure S2 (a,b)). The FSS is more clearly resolved for the XX emission, as the four-particle state is shielded better against Coulomb forces in the QD environment, leading to a spectral broadening of the X emission lines even at lowest excitation power. In this case, a sum of two overlapping Gaussian fits is used to extract the individual linewidths as well as the FSS. This yields values for the FSS under TPE of $83(6)\,\mu\text{eV}$ for the X and $91(2)\,\mu\text{eV}$ for the XX state, in agreement with the results obtained under above-barrier characterization[1] and the value extracted from Figure S1. We obtain linewidths (full-width at half-maximum) of the individual FSS components for the XX- and X-emission of $47(2)\,\mu\text{eV}$ and $119(7)\,\mu\text{eV}$, respectively, and a binding energy of the XX-state of $2.9(1)\,\text{meV}$.

1.4 Effect of weak above-barrier Support

As stated in the main article, the Rabi rotations under two-photon-excitation (TPE) cannot be observed at high excitation powers, as the emission of the exciton (X) and biexciton (XX) is quenched, which also results in deviations of the measured Rabi rotation signal from the theoretical fit at higher pulse areas $> 4\pi$ (cf. main article, Figure 2(a,b)). This behavior is explained as follows: At high pulse areas, the laser generates a large amount of excess charge carriers, which results in dominant emission via the trion state, as an additional charge is always available. This interpretation is confirmed by the observation that introducing additional weak above-barrier excitation(around 780 nm) CW light (not enough to result in noticeable QD emission) to the TPE pulses results in an enhancement of the trion emission, but a quenching of the XX-X emission (see Figure S2(c)). At high excitation powers this effect can occur without additional CW above-barrier support, explaining the reduced X and XX emission intensity at high pulse areas.
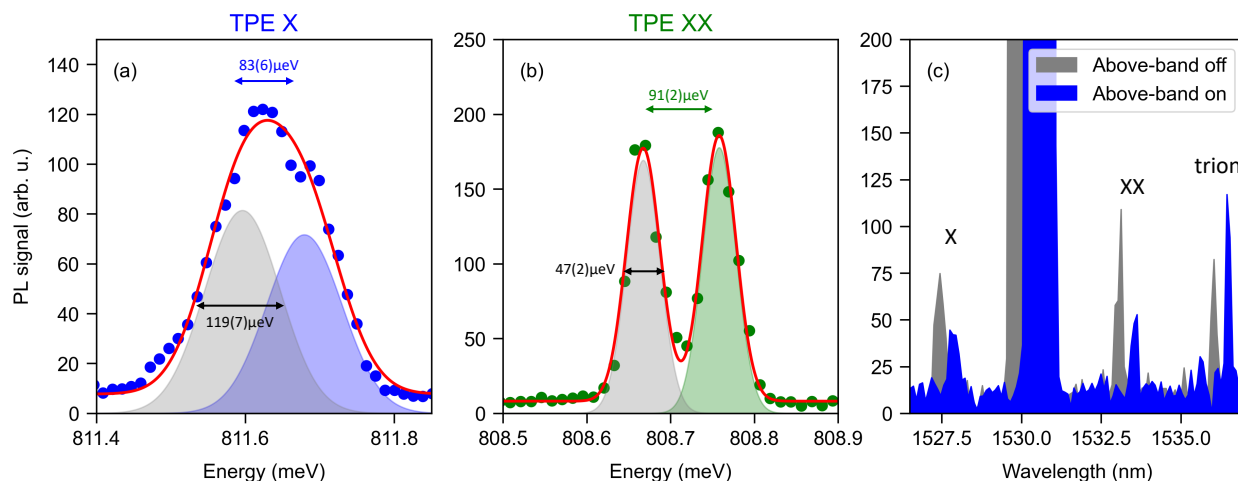

Figure S2: (a,b) Double-Gaussian fits of the X and XX emission under TPE are used to extract the linewidths, fine-structure splitting (FSS), and the XX binding energy. (c) Emission of the QD under TPE without (black) and with (blue) additional weak above-barrier CW excitation, respectively. Data in blue are shifted for better comparison. The partial quenching of the X and XX emission in combination with the enhanced trion signal are indicative for a larger amount of excess charges.

The effect of excess charge carriers is further enhanced by the presence of an unintentional background doping in the sample investigated in our work. The dominant emission of the trion state, not shown in Figure 1(b) in the main article, under above-barrier excitation already indicates

the presence of a large number of intrinsic charge carriers (cf. Figure S3). Interestingly, it has
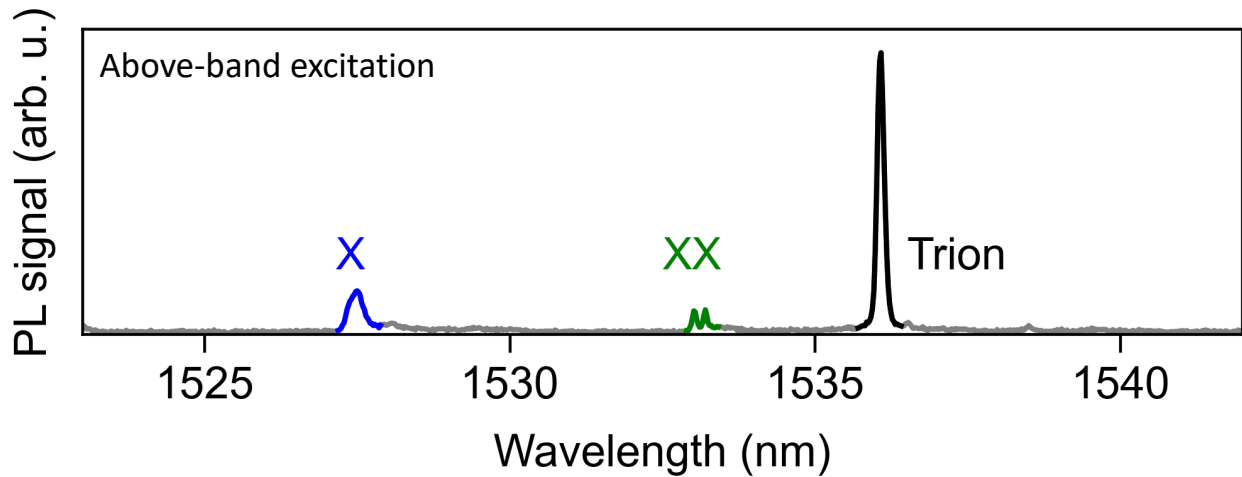

Figure S3: Photoluminescence spectrum under above-barrier excitation with a CW laser at 980 nm. Same spectrum as Figure 1(b) of the main text, but including the dominant trion contribution here.

previously also been reported to be beneficial to add additional weak CW above-barrier excitation, which helped to increase the Rabi rotation amplitude under TPE by saturating the charge environment in Ref. 2. This underlines the sample specific character of effects like intrinsic background doping.

1.5 Comparison of Lifetime Measurements under TPE and above-barrier Excitation

This section provides additional data of the lifetime measurement for the trion state from the QD studied in the main article (see Figure S4(a)), including lifetimes of XX and X-state) and a quantitative comparison of the lifetime measurements for the XX- and X-state under TPE and above-barrier (AB) excitation, respectively (cf. Figure S4(b,c)). The experimental results indicate a slightly reduced decay time under direct coherent excitation via TPE.
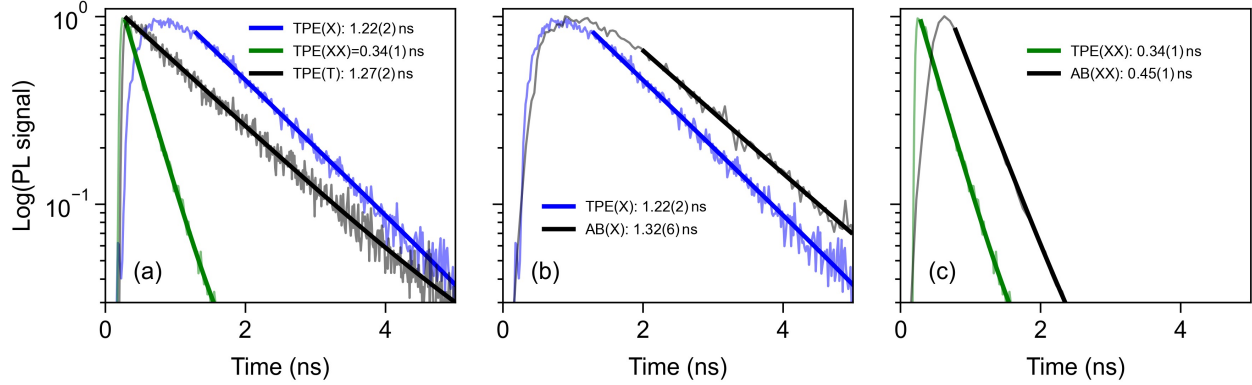
Figure S4: (a) Lifetime measurements for the X-, XX-, and trion- (T) state from the QD studied in the main article. (b) and (c) Comparative study of the XX- and X-lifetimes under pulsed TPE and pulsed above-barrier (AB) excitation.

1.6 Two-Photon Excitation of another QD

This section presents additional data for another QD from the same sample excited via TPE (see Figure S5). The emission of this QD is centered around 1535 nm within the telecom C-band. Figure S5(c) shows the emission spectrum under TPE and the assignment to the respective QD states. The spectral fingerprint of the QD is similar to the one presented in the main article (cf. Figure S5(a)), but smaller emission linewidths below 30 μeV are observed. Note that no additional notch filter was used to suppress the reflected laser in this measurement, resulting in intense laser scattering. The lifetime measurements confirm a 4-times faster decay of the XX-state relative to the X-state (see Figure S5(d)), rendering this type of QD interesting for simultaneously achieving high photon-indistinguishabilities and entanglement fidelities in future work.

2 Evaluation of Preparation Fidelity

2.1 Rabi Fits vs Cross-Correlation

The observation of Rabi rotations in the integrated emission intensity as a function of the excitation power, i.e. pulse area, observed in Figure 2(a,b) of the main article is a signature for the coherent population inversion when using resonant excitation schemes. To extract the preparation
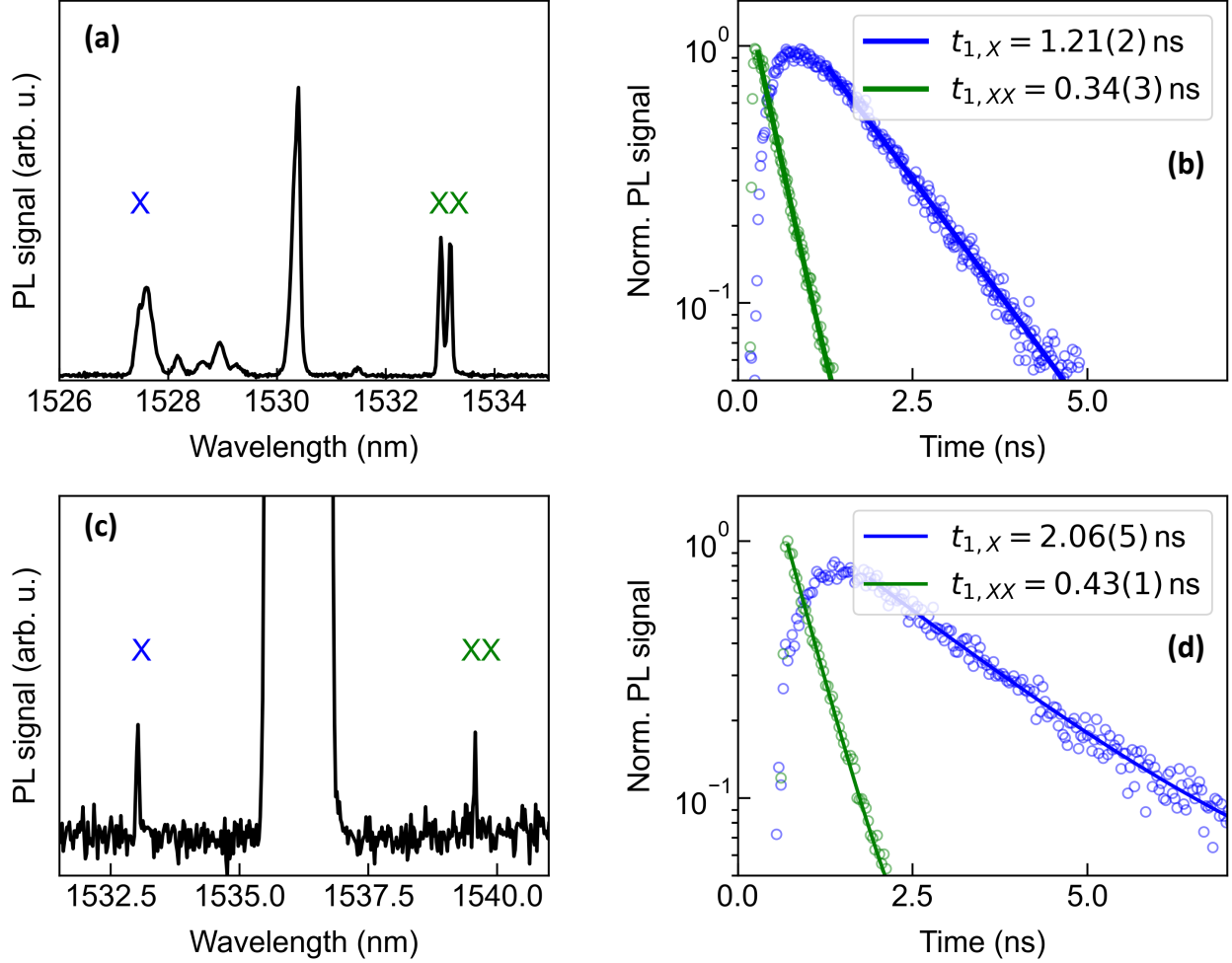
Figure S5: Investigation of a second QD under TPE: (a,b) Emission spectrum and lifetime measurement for the QD from main text for comparison. (c) Emission spectrum and lifetime measurement of another QD from the same sample. (d) Time-resolved measurement of the emission of each QD state under TPE, confirming a 4-times faster decay of the XX state relative to the X-state.

fidelity $\mathscr{F}_{\mathrm{prep}}$ for the upper state quantitatively, we use two different and independent approaches in our work: (1) By fitting the integrated emission intensity as a function of the excitation power using a theoretical model for the Rabi rotations and (2) by performing photon cross-correlation measurements between XX and X photons as a function of the excitation power. As summarized in SI-Table S1 the preparation fidelities extracted using these two approaches agree within the standard error.

For extracting the preparation fidelity from the integrated emission intensity vs. excitation power, we followed the adapted analytical model used in the Supplemental Material of Ref. 3. The

Table S1: Comparison of extracted TPE preparation fidelities using different methods

Method	Preparation Fidelity	Fit Residual
Analytical approx.	82(4)%	0.055
XX-X Cross-Corr.	81(2)%	-

model uses an approximated analytical expression for the Rabi oscillations of a 2-level-system in the time-domain under continuous excitation[4] extended to be applicable for pulsed excitation. The obtained expression describes the occupation probability of the excited state $|c_e|^2$ during the Rabi rotations as a function of pulse area Θ, which for a fixed pulse duration translates into a excitation-power dependence. With the fitting parameter ξ, i.e., the damping rate normalized by the Rabi frequency, the model reads

$$|c_e|^2 = \frac{1}{2\left(1+2\xi^2\right)}\left(1-\left(\cos(\Theta)+\frac{3\xi}{\sqrt{4-\xi^2}}\sin(\Theta)\right)e^{-3\Theta\xi/2}\right),\tag{1}$$

which is used for the fits presented in Figure 2(a,b) of the main article. A preparation fidelity for the XX state of 82(4)% is obtained by extrapolating the exponential envelope function.

To independently verify the result from the Rabi fit, we extracted the preparation fidelity in a second approach via photon cross-correlation measurements between XX and X photons, by comparing the integrated coincidences originating from the same cascade to those of photons from different cascades.[5–7] Such a cross-correlation histogram is depicted in Figure S6(a)) for an excitation power corresponding to a π-pulse. In this measurement, an increasing ratio of center to side peak area corresponds to a decreasing preparation fidelity, i.e., not every laser pulse results in a complete population inversion, leading to bunching in the coincidence histogram. Integrating over all coincidences within the full laser repetition period of 12.5 ns (cf. Figure S6(c)), the preparation fidelity is extracted as:

$$\mathscr{F}_{\text{prep}} = \frac{A_{\text{side}}}{A_{\text{center}}} \cdot C_{\text{Pol}}\tag{2}$$

with A_{side} the average of the integrated coincidences in each of the side peaks, A_{center} the total number of coincidences in the center peak, and C_{Pol} a correction factor accounting for polarized

detection. Concerning the latter, there are some subtleties to consider:

- As we are using a cross-polarized excitation and detection scheme to suppress reflected laser light, the bunching magnitude is 2× larger than without polarization filtering if the horizontally and vertically polarized decay-channels are equally probable (unpolarized source), which needs to be corrected by the re-scaling factor C_{Pol} as done in Ref. 5. In our case, however, the emission of the QD is partially polarized (DOP = 33%, cf. Figure S1(a)), counteracting the effect of polarization filtering in our setup. As a first-order approximation, one may account for a finite DOP by choosing $C_{\mathrm{Pol}} = 2 - \mathrm{DOP}$, resulting in a fully compensated correction factor $C_{\mathrm{Pol}} = 1$ for a fully polarized cascade (DOP = 1). As shown further below (see Figure S8 and associated discussion), simulations reveal a more accurate correction factor of $C_{\mathrm{Pol}} = 1.53$ for our case, which we used to correct the center area (cf. Figure S6(d)).

- Moreover, the QD investigated in this work shows a blinking effect, additionally masking the analysis of the preparation fidelity according to Equation 2. For this reason, we additionally corrected for the blinking by fitting the peak integrals with a double-sided exponential decay (excluding the center coincidence peak), to re-scale the histogram (see Figure S6(e)). This blinking correction was applied for each cross-correlation histogram individually before extracting the preparation fidelity via Eq. 2. Interestingly, evaluating the blinking magnitude as a function of the pulse area, we find that the relative amount of blinking oscillates in phase with the Rabi rotations, while the timescale of the blinking remains constant (cf. Figure S6(b), insets). This can be understood intuitively, as for example a 2π-pulse results in excitation and de-excitation within one laser pulse, thus any blinking cancels out, while at π-power all blinking can be observed.

Note: Correcting for the blinking effect above, even a preparation fidelity $\mathscr{F}_{\mathrm{prep}} = 1$ does strictly not correspond to an on-demand single photon source, as the QD emission is still subject to a random switching between the on- and off-state. We are however confident that such blinking
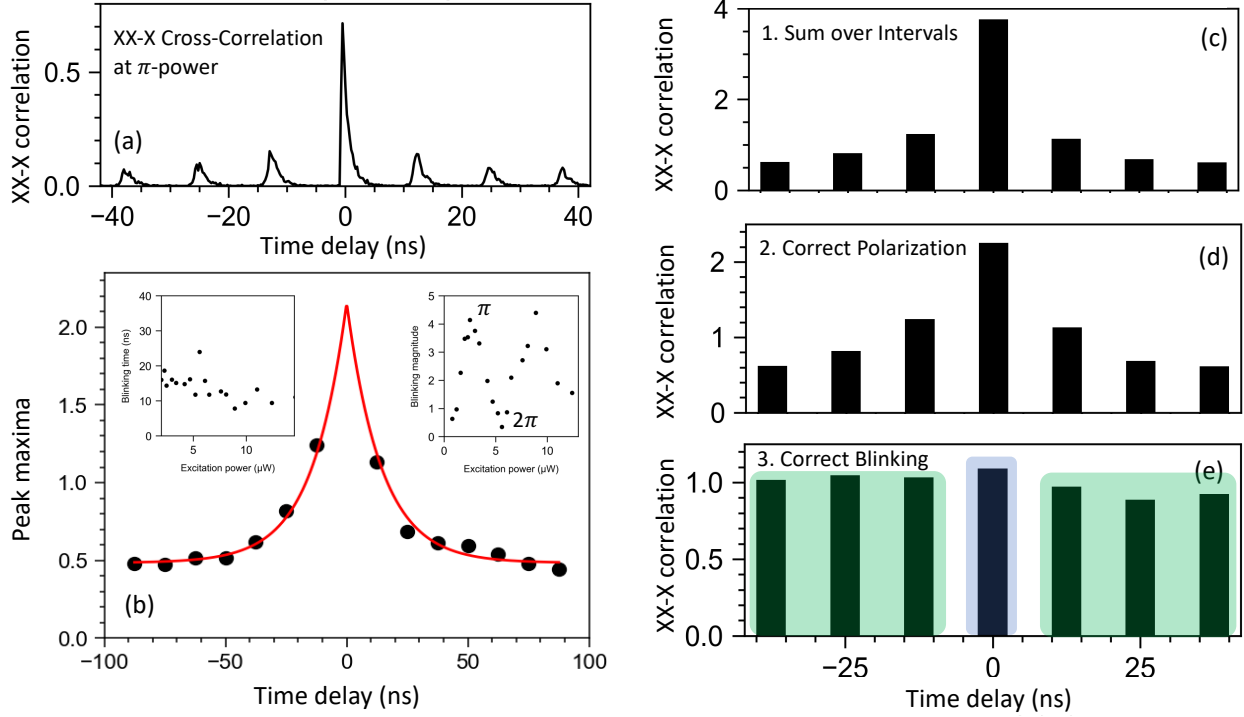
Figure S6: Data evaluation workflow for extracting the preparation fidelity from photon cross-correlation measurements: (a) As-measured XX-X photon cross-correlation histogram under TPE at the π-pulse ($2.5\,\mu$W). (b) Analyzing the blinking effect by fitting a two-sided exponential to the side-peak maxima. Insets: Extracted blinking timescale (left) and blinking magnitude m (right) as a function of the excitation power. To extract the preparation fidelity the following three steps are applied: (c) the coincidences of each peak are integrated within a full repetition period, (d) the center peak is corrected for polarization effects, and (e) the histogram is re-scaled to correct for the blinking. Finally, the preparation fidelity is extracted as the ratio of the average side peak area (green shaded) and the center peak area (blue shaded).

can be controlled by advanced material and device engineering using, e.g., interface passivation or electrical gating.

Applying the analysis discussed above for the experimentally obtained XX-X photon cross-correlation measurements yields a maximum preparation fidelity of 81(2)% under TPE (cf. SI-Table S1 and Figure 3(d) in main article).

To gain further insights in how the excitation scheme affects the preparation fidelity, we additionally performed XX-X photon cross-correlation experiments using pulsed above-barrier excitation (at 1470 nm) at saturation power of the X state ($5\,\mu$W). From the results displayed in Figure S7(a) and (b), we obtain a preparation fidelity of 44(2)%, clearly confirming the sensitive and positive
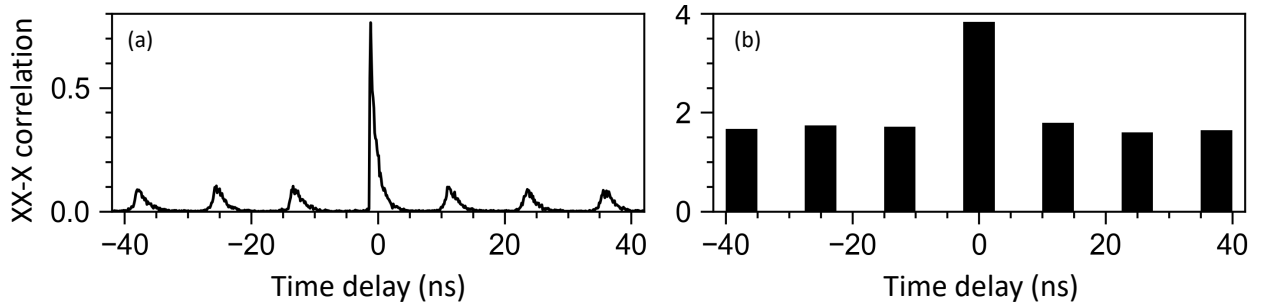
impact of coherent excitation.

Figure S7: Extracting the preparation fidelity under pulsed above-barrier excitation: (a) Raw XX-X photon cross-correlation histogram and (b) integrated coincidences per peak after polarization- and blinking-correction for extraction of the preparation fidelity.

2.2   Additional Simulations of Photon Cross-Correlations

This section provides simulation results enabling the non-trivial polarization correction discussed in SI, Section 2.1. To find the relation between the measured DOP of the QD under study and the required correction factor C_{Pol} in Equation 2, we performed Monte Carlo simulations of the XX-X radiative cascade accounting for the experimentally determined decay times. The simulations directly incorporate the preparation fidelity, i.e., the probability that a laser pulse excites the XX state. The simulation randomly draws between the two possible polarization decay channels (HH or VV) of the cascade, but keeps only results from one decay channel (e.g. horizontal polarizations) to account for the polarization filtering in our experimental setup. Additionally the simulations account for the known experimental imperfections (detector timing jitter, dead time, setup efficiency, etc.), to generate data sets for a representative comparison with our experimental data. Figure S8(a) and (b) shows the simulated cross-correlation histograms for ideal ($\mathscr{F}_{\text{prep}} = 1$) and low ($\mathscr{F}_{\text{prep}} = 0.1$) preparation fidelity for the case of unpolarized emission and without polarization-filtering, respectively. The simulated histograms adequately reproduce the details (coincidence peak asymmetries and area ratios) expected for the QD XX-X cascade. Applying the evaluation workflow presented in Figure S6(c-e) as a cross-check, we retrieve the preparation fidelities originally fed in the simulations in very good approximation. Finally, including the polarization filtering in our simulation

12

and varying the initial DOP, we are able to extract the polarization correction factor C_{Pol} repro-ducing the correct preparation fidelity for each case (cf. Figure S8(c)). The resulting non-linear relation, can be approximated by a quadratic fit, from which we retrieve a polarization correction factor of 1.53 for our case of DOP $= 33\%$ (red circle).
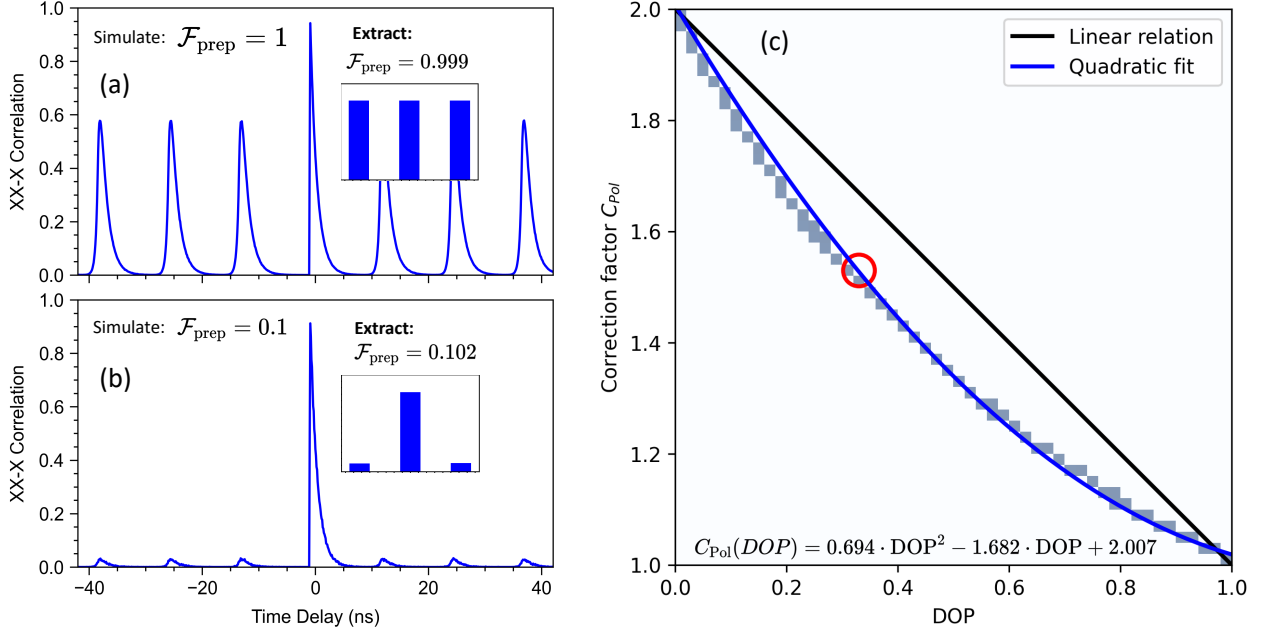

Figure S8: Monte Carlo simulations of the XX-X photon cross-correlation: (a) and (b) Exemplary histograms simulated for perfect ($\mathscr{F}_{\mathrm{prep}} = 1$) and low ($\mathscr{F}_{\mathrm{prep}} = 0.01$) preparation fidelity (excluding polarization effects). Insets in (a) and (b): Applying the data evaluation workflow from Figure S6(c-e) we retrieve the $\mathscr{F}_{\mathrm{prep}}$-values in very good approximation. (c) Correction factor C_{Pol} extracted from the simulations by accounting for the polarization effects discussed in the text. For our experimental conditions of DOP $= 33\%$ a correction factor of $C_{\mathrm{Pol}} = 1.53$ is deduced (red circle) and applied to extract the preparation fidelity from experimental results in Figure 3(d) of the main article.

3 Evaluation of Time-Resolved Measurements

3.1 Extracting Purity from Second-Order Auto-Correlation Measurement

As explained in the main text, the auto-correlation data was fitted with a sum of two-sided mono-exponential decays. We do not apply any background subtraction nor de-convolution with the system's response function, as the measured decay times are about one order of magnitude slower

then the average system response time. We do however account for the blinking effect, by incorporating an exponential envelope function in our fit model as follows

$$C(\tau) = \left[g^{(2)}(0) \cdot e^{-|\tau|/\tau_1} + \sum_{n \neq 0} e^{-|\tau - n\tau_0|/\tau_1} \right] \times C_0 \cdot (1+m) \cdot e^{-|\tau|/\tau_{\text{blink}}} \quad . \tag{3}$$

Here, the normalized coincidences $C(\tau)$ as a function of the detection time delay τ are modelled using the zero-delay coincidences $g^{(2)}(0)$, the radiative decay time τ_1, the laser pulse spacing τ_0, a normalization factor C_0, a blinking timescale τ_{blink} and the blinking magnitude m. The respective best values and standard errors for the parameters are extracted from fits to the experimental data for the X- and XX-state shown in Figure 2(d,e) of the main article (see SI-Table S2). Note, that while for some QDs on this sample, adding some above-barrier light reduced the blinking (indicative of a stabilization of the charge environment), this has not been the case for the QDs studied here. This is in line with the observation that additional above-barrier support increases the amount of excess charges instead of saturating them (cf. SI section 1.4).

The blinking can be used to obtain information about the on/off-ratio as well as a lower bound

Table S2: Fitting parameters for $g^{(2)}$-measurement of XX and X photons under TPE

Parameter	X Fit	XX Fit
decay time τ_1	1.44(1) ns	0.36(1) ns
blinking time τ_{blink}	16.9(3) ns	16.7(3) ns
blinking magnitude m	4.96(7)	3.19(4)
On/Off-times τ_{on} / τ_{off}	20 ns / 100 ns	22 ns / 70 ns
Quantum Efficiency QE	17 %	23 %
center-peak contribution $g^{(2)}(0)$	0.015(4)	0.005(4)

for the quantum efficiency QE. It is a lower bound as random jumping of the emission energy relative to the detected energy can cause on/off-switching that leads to blinking in the auto-correlation measurements reducing the extracted QE, even though the QD still emits a photon. According to Ref. 8, the blinking can be heuristically described by the height h of the m-th. peak maximum obeying $h_{m \neq 0} = 1 + \frac{\tau_{\text{off}}}{\tau_{\text{on}}} \cdot e^{-\left(\frac{1}{\tau_{\text{off}}} + \frac{1}{\tau_{\text{on}}} \right) \cdot |m\tau_0|}$ where τ_{on} and τ_{off} are the on-/off-times of the emitter. This relates to the fitting parameters of our auto-correlation fit (Eq. 3)

via $\tau_{\mathrm{on}} = \left(\frac{1}{1+m}\right)\tau_{\mathrm{blink}}$, $\tau_{\mathrm{off}} = (1+m)\,\tau_{\mathrm{blink}}$ and thus the quantum efficiency can be estimated via $QE = \frac{\tau_{\mathrm{on}}}{\tau_{\mathrm{on}}+\tau_{\mathrm{off}}} = \frac{1}{1+m}$. Using this model, results in an extracted quantum efficiency around 20%. As mentioned in the main text, the extracted blinking envelope function can be used to correct the data for blinking by dividing the data by $(1+m) \cdot e^{-|\tau|/\tau_{\mathrm{blink}}}$. This can be done for the auto-correlation of second order, as well as for the HOM data, which yields blinking-corrected histograms as shown in Figure S9. This is especially useful to confirm that the expected relative ratios of the peak areas in the HOM experiment are reproduced.
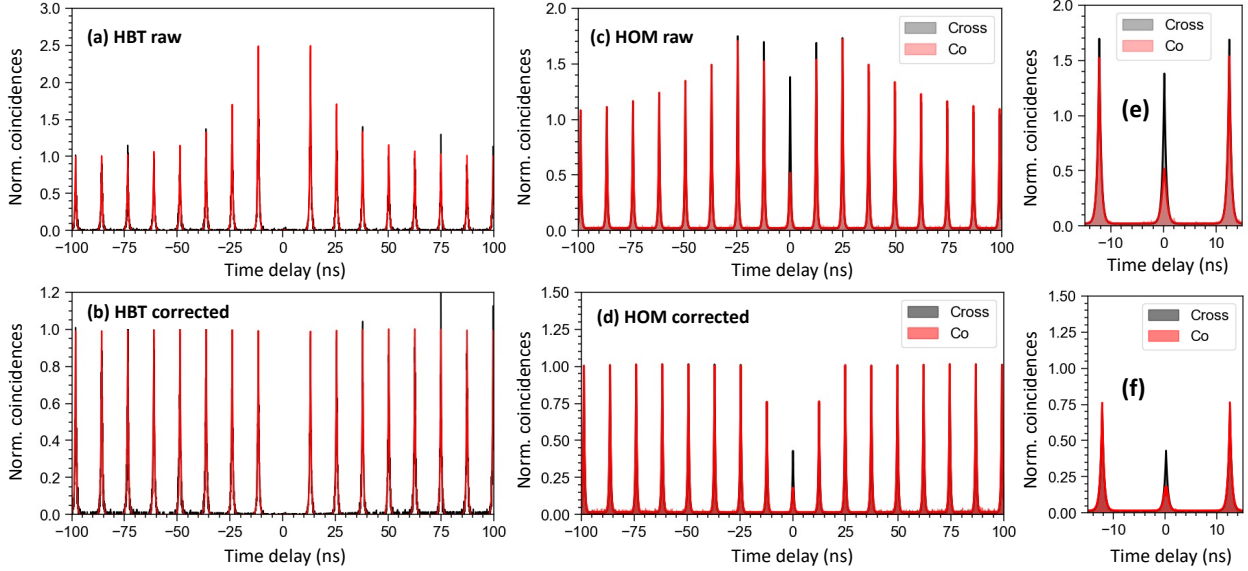

Figure S9: Blinking correction of correlation measurements: (a,b) $g^{(2)}$-data without (top) and with (bottom) blinking correction. Data (black) is shown together with fit according to Eq. 3 (c,d) Correcting blinking for the HOM data reproduces the expected peak heights for HOM experiments with 12.5 ns delay. Cross-polarized (grey) and co-polarized (red) data is shown together with the fit according to Eq. 4. (e,f) close-up of HOM data without and with blinking correction.

3.2 Extracting Indistinguishability from HOM Measurement

To extract the two-photon interference visibility as a measure for the photon indistinguishability from Hong-Ou-Mandel (HOM) measurements, different methods can be applied. Using only the co-polarized measurement data and comparing center to side peak areas is not precise in the presence of blinking. Hence, to evaluate our HOM measurements we compare the co-polarized

measurement with a maximally distinguishable cross-polarized reference measurement. In order to compare both measurements, they are fitted according to equation

$$C_{\text{co}}(\tau) = \left[A \cdot e^{-|\tau|/\tau_1} \left(1 - V_{\text{PS}} e^{-|\tau|/\tau_2} \right) + \sum_{n \neq -1,0,1} e^{-|\tau + n\tau_0|/\tau_1} + \frac{3}{4} \left(e^{-|\tau + \tau_0|/\tau_1} + e^{-|\tau - \tau_0|/\tau_1} \right) \right]$$
$$\times C_0 \cdot (1 + m) \cdot e^{-|\tau|/\tau_{\text{blink}}}$$

for the co-polarized data and

$$C_{\text{cross}}(\tau) = \left[A \cdot e^{-|\tau|/\tau_1} + \sum_{n \neq -1,0,1} e^{-|\tau + n\tau_0|/\tau_1} + \frac{3}{4} \left(e^{-|\tau + \tau_0|/\tau_1} + e^{-|\tau - \tau_0|/\tau_1} \right) \right]$$
$$\times C_0 \cdot (1 + m) \cdot e^{-|\tau|/\tau_{\text{blink}}}$$

for the corresponding cross-polarized data. Here A captures the area of the center peak, V_{PS} is the post-selected visibility value that is set to zero for fitting the cross-polarized data, τ_1 the decay time and τ_2 the coherence time. The blinking is included in the same way as in the $g^{(2)}$-fit (Eq. 3) with the blinking amount m and timescale τ_{blink} and a normalization factor C_0. Note that we do not subtract any background or correct for limited purity here as the $g^{(2)}$-measurement confirmed the good suppression of the reflected laser light. After fitting both co- and cross-polarized data, the data is divided by the normalization constant C_0, which ideally should be 1, but insufficient statistics sometimes leads to imperfect normalization. In this way both measurements are normalized to their respective Poisson levels. The fitting parameters of the HOM fit of the XX photons for co- and cross-polarized measurement are collected in SI-Table S3.

After confirming the normalization of the date by finding $C_0 = 1$, the coincidences within a 4 ns time window for the co- as well as for the cross-polarized data are integrated and the visibility is computed as $V_{\text{HOM}} = 1 - \frac{A_{\text{co}}}{A_{\text{cross}}}$. The size of the integration window influences the value of V_{HOM}. As discussed in the main text, using a reduced integration window instead of the full laser period of 12.5 ns improves the signal-to-noise-ratio, especially as the count rate was relatively low in our

16

Table S3: Fitting parameters for HOM-measurement of XX photons

Parameter	Cross-polarized	Co-polarized
normalization constant C_0	1.000(1)	0.999(1)
decay time τ_1	0.36(1) ns	0.36(1) ns
blinking time τ_{blink}	23(1) ns	32(2) ns
blinking contribution m	2.05(5)	1.41(5)
post-selected indistinguishability V_{PS}	-	73(6)%
coherence time τ_2	-	0.15(5) ns
Normalized integrated coincidences $A_{4\text{ns}}$	3.88	2.48

experiments, but does not correspond to any post-selection yet as about 99% of the coincidence data lie within the 4 ns integration window (see Figure S10(a)). Thus, only reducing the window further than 4 ns improves V_{HOM} super-linearly via post-selection. Therefore, we state also the 4 ns integration window in the main article, to also compare better to previous works using the same integration window.

The effect of changing the integration time window is illustrated in Figure S10(b), where the transition from the regime in which only the signal-to-noise-ratio is improved to the post-selection regime can be readily observed. We have indicated the 4 ns time window (black dashed line) and the previous record of InP indistinguishability obtained with that integration time window[9] (red dashed line), that is clearly surpassed by using coherent excitation.
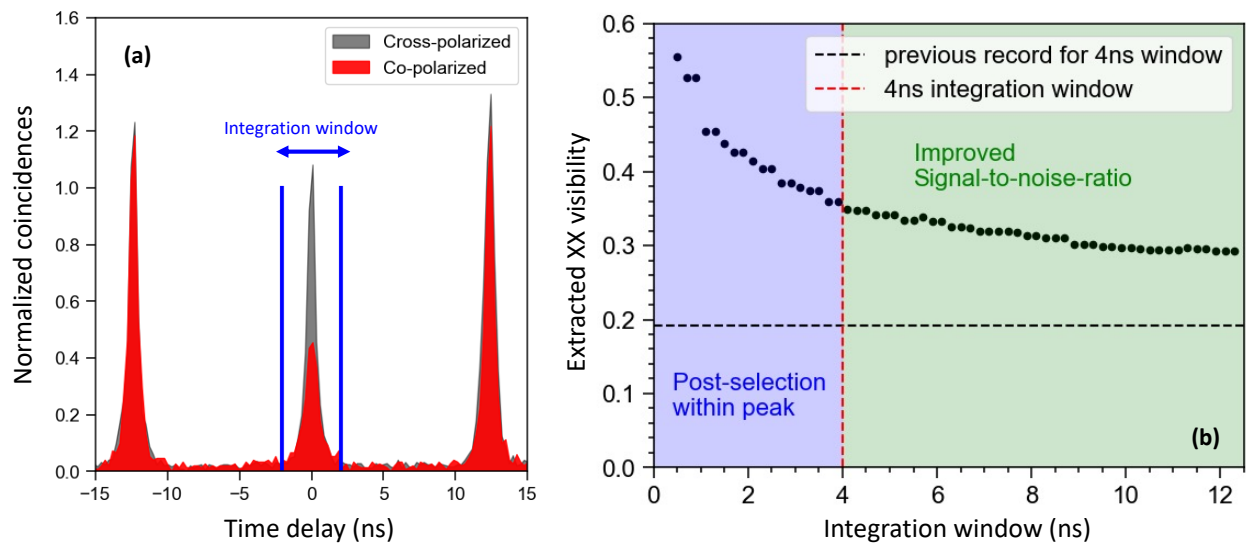
Figure S10: (a) The majority of the coincidence data lies within a 4 ns time window. (b) Different integration time windows lead to different extracted V-values as for windows > 4 ns the background emission contributes and for windows < 4 ns the data is post-selected. For all integration windows we improve over the previous state-of-the-art for C-band QDs (black dashed line).[9]

References

(1) Holewa, P.; Sakanas, A.; Gür, U. M.; Mrowiński, P.; Huck, A.; Wang, B.-Y.; Musiał, A.; Yvind, K.; Gregersen, N.; Syperek, M.; Semenova, E. Bright quantum dot single-photon emitters at telecom bands heterogeneously integrated on Si. *ACS Photonics* **2022**, *9*, 2273–2279.

(2) Zeuner, K. D.; Jöns, K. D.; Schweickert, L.; Reuterskiöld Hedlund, C.; Nuñez Lobato, C.; Lettner, T.; Wang, K.; Gyger, S.; Schöll, E.; Steinhauer, S.; Hammar, M.; Zwiller, V. On-Demand Generation of Entangled Photon Pairs in the Telecom C-Band with InAs Quantum Dots. *ACS Photonics* **2021**, *8*, 2337–2344.

(3) Pennacchietti, M.; Cunard, B.; Nahar, S.; Zeeshan, M.; Gangopadhyay, S.; Poole, P. J.; Dalacu, D.; Fognini, A.; Jöns, K. D.; Zwiller, V., et al. Oscillating photonic Bell state from a semiconductor quantum dot for quantum key distribution. *arXiv preprint arXiv:2307.06473* **2023**, (accessed 20-12-2023).

(4) Fox, A. M. *Quantum optics: an introduction*; Oxford University Press, USA, 2006; Vol. 15.

(5) Wang, H.; Hu, H.; Chung, T.-H.; Qin, J.; Yang, X.; Li, J.-P.; Liu, R.-Z.; Zhong, H.-S.; He, Y.-M.; Ding, X., et al. On-demand semiconductor source of entangled photons which simultaneously has high fidelity, efficiency, and indistinguishability. *Physical review letters* **2019**, *122*, 113602.

(6) Rota, M. B.; Basset, F. B.; Tedeschi, D.; Trotta, R. Entanglement teleportation with photons from quantum dots: toward a solid-state based quantum network. *IEEE Journal of Selected Topics in Quantum Electronics* **2020**, *26*, 1–16.

(7) Neuwirth, J.; Basset, F. B.; Rota, M. B.; Hartel, J.-G.; Sartison, M.; da Silva, S. F. C.; Jöns, K. D.; Rastelli, A.; Trotta, R. Multipair-free source of entangled photons in the solid state. *Physical Review B* **2022**, *106*, L241402.

(8) Santori, C.; Pelton, M.; Solomon, G.; Dale, Y.; Yamamoto, Y. Triggered single photons from a quantum dot. *Physical Review Letters* **2001**, *86*, 1502.

(9) Holewa, P.; Zięba-Ostój, E.; Vajner, D. A.; Wasiluk, M.; Gaál, B.; Sakanas, A.; Burakowski, M.; Mrowiński, P.; Krajnik, B.; Xiong, M., et al. Scalable quantum photonic devices emitting indistinguishable photons in the telecom C-band. *arXiv preprint arXiv:2304.02515* **2023**, (accessed 20-12-2023).